Subpicosecond carrier dynamics in low-temperature grown GaAs as measured by time-resolved terahertz spectroscopy

Matthew C. Beard, Gordon M. Turner, and Charles A. Schmuttenmaer[a)]
Chemistry Department, Yale University, 225 Prospect Street, P.O. Box 208107, New Haven, Connecticut 06520-8107

(Received 23 March 2001; accepted for publication 10 September 2001)

The transient photoconductivity in a 1 μm layer of low temperature grown GaAs (LT-GaAs) on a GaAs substrate was measured using time-resolved terahertz spectroscopy. When photoexcitation occurs at 400 nm we find a time-dependent mobility that increases from 400 ± 100 to 1100 ± 100 cm^2 V^{-1} s^{-1} with a time constant of 2 ps. Photoexcitation at 800 nm produces a time-independent mobility of 3000 ± 500 cm^2 V^{-1} s^{-1}. We determine the carrier lifetime in LT-GaAs to be 1.1 ± 0.1 ps. © *2001 American Institute of Physics.* [DOI: 10.1063/1.1416140]

I. INTRODUCTION

Low-temperature grown GaAs (LT-GaAs) is a semiconducting material with a high carrier mobility and a fast carrier capture time. The mobility is larger than in silicon[1] and almost as large as in regular GaAs, while the carrier lifetime is three orders of magnitude smaller; ~1 ps in LT-GaAs (Ref. 2) compared to ~1 ns in GaAs (Ref. 3) and ~10 ms in silicon.[4] This makes LT-GaAs materials attractive for applications such as ultrafast switches and terahertz antennas; applications for which it is desirable to have the highest possible mobility with the shortest possible carrier lifetime. In this work, we use time-resolved THz spectroscopy (TRTS) to study the carrier mobility after photoexcitation. Time-resolved THz spectroscopy enables the quantitative determination of the conductivity, a product of the carrier mobility and carrier density, on a subpicosecond time scale. No other technique allows for such a determination on these time scales.

Low-temperature grown GaAs is produced using molecular beam epitaxy (MBE) of GaAs at low substrate temperatures during growth in an excess As flux, $T_g = 180-300$ °C, followed by a high temperature anneal, $T_a = 400-800$ °C, for a short period of time, $t_a = 1-30$ min. Before annealing, the as-grown material is highly nonstoichiometric, containing excess As, and its properties are governed by point defects such as As interstitials and As antisites.[5] Photoexcitation of the as-grown material results in subpicosecond carrier lifetimes. Furthermore, the as-grown material is conductive in its nonphotoexcited state.[6] The material properties, however, change dramatically upon annealing due to the precipitation of As clusters. The point defects are reduced as the excess As precipitates in an Ostwald ripening process.[5] The material can then be best described as a mixture of metallic As clusters embedded in a GaAs semiconductor matrix.

Control of the As cluster size and the distance between clusters is accomplished by varying the anneal temperature and time, T_a and t_a, respectively.[7] Annealing reduces the number of point defects, and also increases the distance between As islands. Since photoexcited electrons can be trapped by As clusters acting as buried-Schottky barriers,[5] or by residual EL-2-like point defects,[8] photoexcited carrier lifetimes increase with increasing anneal temperature and time,[5,7] but still remain much shorter than in regular GaAs. Furthermore, the mobility increases over the as-grown material upon annealing because the defects and lattice strain are decreased.

There has been a great deal of recent interest in generation, propagation, and detection of fs-THz pulses.[9–15] One of the most unique attributes of this new spectroscopic method is that it allows time-resolved studies to be carried out in the far-infrared (FIR) region of the spectrum with subpicosecond temporal resolution. Due to difficulties in carrying out and interpreting experiments based on *time-resolved* THz spectroscopy, reports of them are less numerous than reports utilizing THz pulses in a non-time-resolved mode, often referred to as THz time-domain spectroscopy (THz-TDS). However, in this article we show that TRTS is a powerful technique for studying the subpicosecond evolution of the far-infrared spectrum after photoexcitation, and we apply it to study the photoconductivity in LT-GaAs.

II. EXPERIMENT

The experimental apparatus has been described previously,[3] and will not be repeated here. The sample, purchased from MellWood Laboratories, Inc., consists of a 1 μm thick LT-GaAs layer on top of a 50 nm $Al_{0.6}Ga_{0.4}As$ barrier deposited on a semi-insulating GaAs substrate. After MBE growth the sample was annealed *in situ* for 30 min at 550 °C with an arsenic flux. Experiments were done with photoexcitation wavelengths of 400 and 800 nm. The optical penetration depth depends strongly on wavelength,[16] such that photoexcitation at 400 nm excites electrons solely within the LT-GaAs layer, while 800 nm photons penetrate further and excite electrons in the GaAs substrate as well. For 400 nm excitation, the fundamental laser output was frequency doubled in a 1 mm thick β-BaB_2O_4 (BBO) crystal, and an intensity of 0.9 μJ cm^{-2} per pulse was used to excite the

a)Electronic mail: Charles.schmuttenmaer@yale.edu

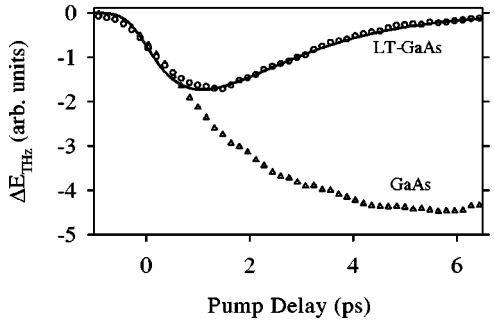

FIG. 1. 1D pump scans of LT-GaAs compared to GaAs when photoexcited at 400 nm.

sample. The spot size was 1.0 cm^2, and was about two times larger than the spot size of the THz pulse. The 800 nm pump pulse energy was 0.3 $\mu J\ cm^{-2}$, with a 1.5 cm^2 spot size. The experiments were done under a dry nitrogen purge at room temperature.

Complete methods for collecting and interpreting the data are described in the supplementary Electronic Physics Auxiliary Publication Service (EPAPS) deposit that accompanies this article.[17] This supplementary material describes how the data must be properly collected and analyzed in order to extract the far-infrared spectrum. This includes deconvolution of the detector response function in order to maximize the temporal resolution. In addition, to extract quantitative values of the conductivity, the THz beam path must be described accurately. This entails specification of all the interfaces that the THz beam encounters, as well as the spatial distribution of the photoexcited carriers, which can be obtained by solving the appropriate diffusion equations. Finally, the nonphotoexcited optical properties of the medium in the far-infrared must be known. When all these effects are properly accounted for, the frequency-dependent conductivity $\sigma(\omega;t'')$ is obtained without assumption of a model at each pump delay time, t''.

The effective mass of hole carriers in GaAs is known to be seven times greater than that of electrons.[1] We assume this to be true for LT-GaAs as well, and therefore only consider photoexcited electrons as contributing to our observed signal.

III. RESULTS

A. 400 nm excitation

Photoexcitation with 400 nm (3.1 eV) light produces carriers with approximately 1.6 eV excess energy at 300 K. These photoexcited carriers have enough energy to undergo intervalley scattering since the *L* and *X* valley minima are 0.3 and 0.46 eV above the Γ valley minimum, respectively.[18] Conduction electrons in either the *L* or *X* valley have a much lower mobility than electrons in the Γ valley. Since higher mobilities result in greater THz absorption, we are less sensitive to electrons in the *L* and *X* valleys, and our measured data reflect the dynamics of the electrons returning to the Γ valley at this excitation wavelength. Figure 1 shows the results of photoexciting GaAs and LT-GaAs at 400 nm while monitoring the highest point on the THz waveform. The intensity of the pump pulse was held constant for both scans, thus, differences in the observed signals are due solely to differences between the conductivity of LT-GaAs and regular GaAs. The onset of photoconduction is nearly identical in both cases, but the LT-GaAs scan shows a subsequent rapid decrease in THz absorption corresponding to trapping of the photogenerated carriers by the As clusters.

Stanton and Bailey[19] modeled the onset of photoconductivity with three states. One state represents the combined *L* and *X* valleys, and there are two states for the Γ valley: an upper state and a lower state. Carriers are photoexcited into the upper Γ state and rapidly scatter (10 fs) into the *L* and *X* valleys. They can then scatter back to the upper Γ state, but the rate at which they relax is governed by the relaxation rate from the upper Γ state to the lower Γ state, and only those carriers in the lower Γ state are allowed to contribute to the signal. Once in the lower Γ state they cannot scatter out. We then multiplied these model dynamics by an exponentially decreasing function to describe the trapping process in LT-GaAs, and finally, we convoluted the model with a Gaussian function to represent the visible pulse width. A nonlinear least squares fit of the model to the data was performed and the results are shown as the solid line in Fig. 1. We find that the relaxation time from upper to lower Γ states τ_Γ in LT-GaAs is 2 ± 1 ps, the carrier lifetime τ_l is 1.3 ± 0.1 ps, and the full width at half maximum (FWHM) of the Gaussian function is 680 fs. This is larger than the FWHM of the excitation pulse because it is based on a fit to a 1D scan (we only monitored one point on the THz waveform), rather than a 2D grid of data (collecting a full THz scan at each pump-delay time) as is presented below.

Figure 2 displays the observed real and imaginary parts of the frequency-dependent complex conductivity ($\mathrm{Re}[\sigma]$ and $\mathrm{Im}[\sigma]$) in LT-GaAs photoexcited at 400 nm, as a function of pump-delay time t'' from -1 to 3 ps.[20] To obtain $\sigma(\omega;t'')$ we treat the photoexcited sample as a dielectric stack of air/photoexcited LT-GaAs/nonphotoexcited LT-GaAs as discussed in detail in Refs. 3 and 17. The photoexcited carrier path length is given by the optical skin depth at 400 nm, which we assume to be the same as that of GaAs, and is 14 nm.[16]

The $\mathrm{Re}[\sigma]$ is essentially independent of frequency for all pump-delay times; it rises to its maximum in about 1 ps, and then decays exponentially back to zero. The $\mathrm{Im}[\sigma]$ is frequency dependent, and rises at the lower frequencies for the first ~ 0.5 ps and then rises rapidly at higher frequencies. The overall maximum occurs concurrently with that for $\mathrm{Re}[\sigma]$, at about 1 ps. At each pump-delay time, the $\mathrm{Im}[\sigma]$ shows very little curvature as a function of frequency, which implies that its peak lies beyond our spectral coverage.

While the measured $\mathrm{Re}[\sigma]$ and $\mathrm{Im}[\sigma]$ are obtained without assuming a model, it is useful to employ one to describe and understand the transient conductivity. The simplest model of conductivity is the Drude model, which treats conduction electrons as free to move under the influence of an applied field, subject only to a collisional damping force.[21] In this model, the probability of a collision during an interval dt is dt/τ_{coll}, where τ_{coll} is the scattering time, or equivalently, the average time between collisions. The collisions cause a

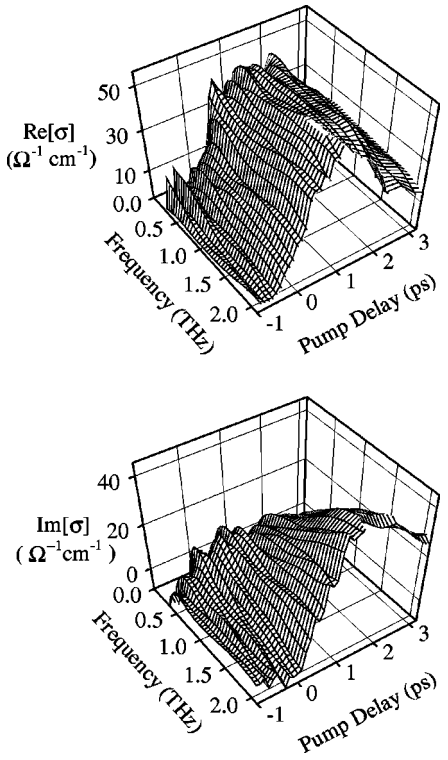

FIG. 2. Measured time-resolved frequency-dependent complex conductivity, Re[σ] and Im[σ], in LT-GaAs photoexcited at 400 nm. A color representation of this figure, along with a comparison to ΔOD and $\Delta\phi$, is available in the EPAPS repository (see Ref. 20).

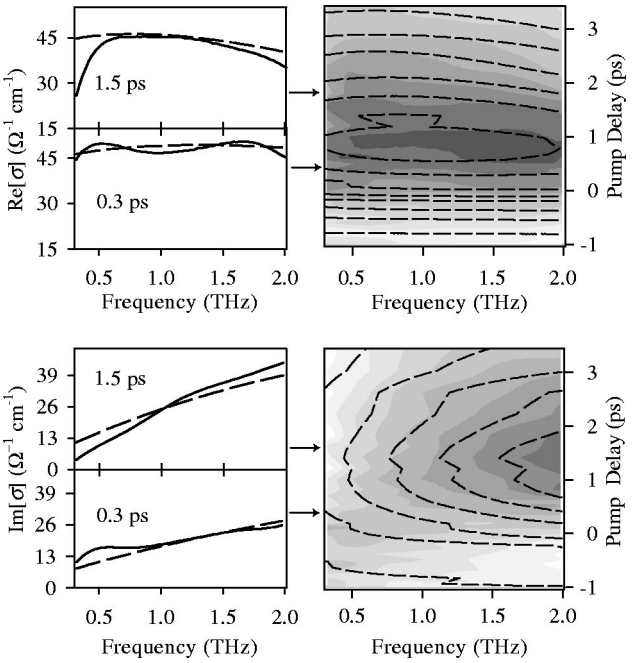

FIG. 3. The calculated model vs the measured complex conductivity in LT-GaAs, Re[σ] and Im[σ], photoexcited at 400 nm. The model is based on the generalized Cole–Cole Drude (GCCD) model of conductivity. The dashed contour lines are the calculated values and the shaded contours are the measured data shown in Fig. 2. Two cuts of the data are shown at the left, one at 0.3 ps and one at 1.5 ps, where the measured data are shown with solid lines, and the calculated data with dashed lines. A color representation of this figure is available in the EPAPS repository (see Ref. 20).

momentum dephasing, so τ_{coll} is sometimes referred to as the dephasing time. We have found that this simple model cannot fully account for the frequency-dependent conductivity in regular GaAs.[3] Not surprisingly, the Drude model must also be modified in order to fit the observed conductivity in LT-GaAs. Generalization of the Drude model is accomplished by allowing a continuous distribution of relaxation times.[3,22] We generalize the Drude model through modifications analogous to the ''Cole–Cole''[23] (CC) modifications of the Debye model for liquids.[24,25] This results in an additional parameter, α, that specifies the breadth of the distribution of scattering times.[3,26] The equation for the generalized Cole–Cole Drude (GCCD) model is as follows:

$$\sigma(\omega)=\frac{\varepsilon_{\mathrm{o}}\omega_p^2\tau_{\mathrm{o,coll}}}{1-(i\omega\tau_{\mathrm{o,coll}})^{1-\alpha}}, \tag{1}$$

where ε_{o} is the free space permittivity, $\tau_{\mathrm{o,coll}}$ is the critical scattering time, α is the CC parameter, and ω_p is the plasmon frequency (defined as $\omega_p^2=Ne^2/(\varepsilon_{\mathrm{o}}m^*)$, where N is the carrier density). When $\alpha=0$ we recover the Drude model. The critical scattering time $\tau_{\mathrm{o,coll}}$ is equal to the average scattering time $\langle\tau_{\mathrm{coll}}\rangle$ for this model. Additionally, the peak of Im[σ] occurs at radial frequency $\omega=1/\tau_{\mathrm{o,coll}}$. The mobility is related to the average scattering time by $\mu=e\langle\tau_{\mathrm{coll}}\rangle/m^*$, where e is the charge of the carrier, and m^* is its effective mass.

We fit the GCCD model simultaneously to the entire grid of Re[σ] and Im[σ] by parameterizing the carrier density $N(t)$ as a function of pump-delay time. The carrier density is obtained by using the same type of model described above for the 1D pump scans. We assume that τ_Γ is the same as that obtained from the 1D results, and do not vary this parameter when fitting the model to the data. We vary the maximum carrier density, N_{o}, the carrier lifetime, τ_l (not to be confused with the scattering time τ_{coll}), the CC parameter α, and the FWHM of the Gaussian function, for the entire data set. Then, for each pump-delay time we vary the critical scattering time $\tau_{\mathrm{o,coll}}$ while the global parameters enumerated above are held fixed. For pump-delay times less than 0.3 ps, the data are not described well by the GCCD model. A more complete model at these pump-delay times would account for having both the visible and THz pulses overlapped temporally in the sample.[3]

Figure 3 shows the fit of the model to Re[σ] and Im[σ]. Two representative cuts at pump-delay times of 0.3 and 1.5 ps are also shown, and the parameters from the fit are summarized in Table I. The uncertainty of the extracted mobilities is about 5%, and for the carrier densities it is about 2%. We find that the carrier lifetime is 1.1 ± 0.1 ps and that the Gaussian FWHM, a measure of our temporal resolution, is 220 fs. These values are slightly different than those observed with the 1D pump scans, and the reason for this is that there is more information contained in the full 2D grid. The 1D pump scan only measures a single point on the THz waveform, whereas the complete underlying dynamics are extracted from the 2D data set.

The extracted mobility as a function of pump-delay time is shown in Fig. 4. The mobility is initially low and then

TABLE I. Summary of the results from this study. The results are grouped by figure. Units for mobility, μ, are $cm^2\ V^{-1}\ s^{-1}$, and the reported values have an estimated error of $\pm 5\%$.

400 nm	800 nm
Fig. 1	**Fig. 6**
$\tau_l = 1.3 \pm 0.1$ ps	$\tau_l = 1.1 \pm 0.1$ ps
$\tau_\Gamma = 2 \pm 1$ ps	offset $= 36.8 \pm 0.2\%$
$\Delta w = 680$ fs	$\Delta w = 700$ fs
Fig. 3	**Fig. 8**
$N_o = 4.6 \pm 0.1 \times 10^{17}\ cm^{-3}$	$N_o = 2.7 \pm 0.2 \times 10^{16}\ cm^{-3}$
$\tau_l = 1.1 \pm 0.1$ ps	$\tau_l = 1.4 \pm 0.1$ ps
$\Delta w = 220$ fs	$\Delta w = 250$ fs
$\tau_\Gamma = 2 \pm 1$ ps (fixed)	offset $= 26 \pm 1\%$
$\alpha = 0.54$	$\alpha^{a} = 0.48$
	$\alpha^{b} = 0.5$
	$\mu^{b} = 7300$ ($t = 0$ ps)
	$\mu^{b} = 9700$ ($t > 4$ ps)
	$\tau_\mu{}^{b} = 2.0 \pm 0.2$ ps
Selected cuts of Fig. 3	**Selected cuts of Fig. 8**
at 300 fs	**at 300 fs**
$N = 4.5 \times 10^{17} cm^{-3}$	$N^{a} = 2.5 \times 10^{16}\ cm^{-3}$
$\mu = 500$	$\mu^{a} = 3200$
	$N^{b} = 6.7 \times 10^{15} cm^{-3}$
	$\mu^{b} = 7500$
at 1.5 ps	**at 1.5 ps**
$N = 2.7 \times 10^{17} cm^{-3}$	$N^{a} = 1.1 \times 10^{16}\ cm^{-3}$
$\mu = 1100$	$\mu^{a} = 3000$
	$N^{b} = 7.3 \times 10^{15} cm^{-3}$
	$\mu^{b} = 8100$
Fig. 4	**Fig. 9**
$\tau_\mu = 2.0 \pm 0.2$ ps	$\mu^{a} = 3000$
$\mu = 392$ ($t = 0$ ps)	
$\mu = 1300$ ($t > 2$ ps)	

[a]LT-GaAs.
[b]GaAs.

increases for about two picoseconds before leveling off. A functional form of an exponential rise to a maximum with an offset, $\{\mu = \mu_i + \mu_f[1 - \exp(t/\tau_\mu)]\}$, was fit to the data, where μ_i is the mobility offset, μ_f is the amount it changes, and the time constant τ_μ was found to be 2.0 ± 0.2 ps.

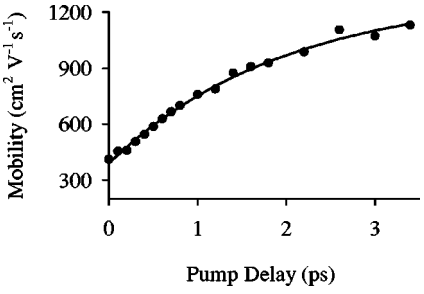

FIG. 4. The extracted values of the mobility (dots) as a function of pump-delay time. The line is an exponential rise to a maximum function fit to the data with a time constant of 2.0 ps.

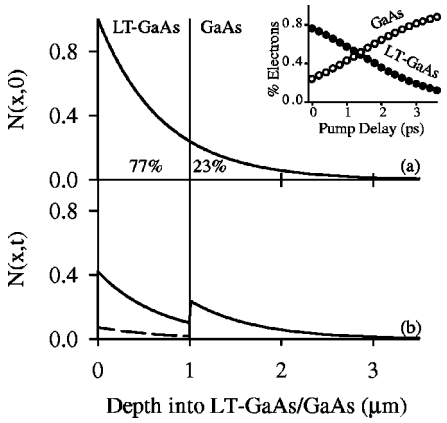

FIG. 5. Carrier density profiles for photoexcitation at 800 nm at three different pump-delay times. (a) Is the initial carrier density distribution at $t'' = 0$ and is exponential. The vertical line indicates the LT-GaAs/GaAs boundary. (b) Shows plots of the carrier density at $t'' = 1$ ps (solid line) and $t'' = 3$ ps (dashed line). The inset displays the percentage of electrons in the LT-GaAs layer (filled circles) and GaAs layer (empty circles) as a function pump-delay time.

B. 800 nm excitation

The situation is different with 800 nm photoexcitation because the 0.7 μm optical skin depth[16] is on the order of the 1 μm thickness of the LT-GaAs layer, and 23% of the initial photoexcited carrier density is therefore in the GaAs substrate. Figure 5(a) displays the spatial distribution of excited carriers immediately after photoexcitation. Bulk recombination occurs very slowly in GaAs (>1 ns) and the spatial distribution of carriers in the GaAs region remains fixed on the time scale of 1–10 ps. However, carriers generated in the LT-GaAs layer are rapidly trapped in less than 2 ps. Figure 5 (b) plots the carrier density profiles at pump-delay times of 1 and 3 ps. These density profiles were determined numerically using a diffusion model with reflecting boundaries[3,27,28] at the LT-GaAs/GaAs interface to account for the insulating $Al_{0.6}Ga_{0.4}As$ barrier, and this model is used to determine the relative fraction of electrons remaining in the LT-GaAs layer. As the electrons in LT-GaAs are trapped, their overall density decreases relative to the density of electrons in GaAs. The inset of Fig. 5 shows the relative population of excited carriers in LT-GaAs and GaAs as a function of pump-delay time. After 1.2 ps there are more excited carriers remaining in the GaAs substrate than in the LT-GaAs layer.

Figure 6 shows the results of a 1D pump scan (scanning

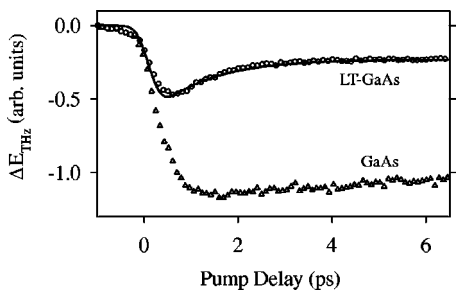

FIG. 6. 1D pump scans of LT-GaAs compared to GaAs, both photoexcited at 800 nm.

pump with a fixed probe-delay time) of LT-GaAs with 800 nm photoexcitation compared to that for regular GaAs. The data set for photoexcitation of LT-GaAs shows a sharp decrease in the THz transmission followed by a rapid increase (similar to photoexcitation at 400 nm shown in Fig. 1), but levels off with a 1.3 ps time constant rather than achieving a complete recovery. The origin of the long-time offset is the presence of excited carriers in the GaAs substrate, which do not decay on this time scale. The solid line in Fig. 6 is the result of a 700 fs FWHM Gaussian function convoluted with an exponential decay having a long-time offset that was fit to the data. The decay time constant is 1.1 ± 0.1 ps and the offset is 37% of the maximum. Note that the offset is greater than 23% (the relative population of carriers excited into GaAs vs LT-GaAs) because the carriers in GaAs have higher mobility and absorb more of the THz probe beam than do the carriers in LT-GaAs, and thus contribute to a larger percentage of the signal.

Even though we can calculate the relative excited electron populations in LT-GaAs and GaAs as a function of pump-delay time, as shown in the inset of Fig. 5, it is not possible to extract the conductivity solely in the LT-GaAs layer and/or GaAs substrate in the absence of a model. Similar difficulty will be encountered for any system in which more than one layer of the dielectric stack changes upon photoexcitation. This is in contrast to photoexcitation at 400 nm, where we extract the conductivity in LT-GaAs directly because the absorption skin depth is too short to excite carriers in the GaAs substrate. As a result, we report the complex conductivity of LT-GaAs photoexcited at 400 nm, but only report the change in optical density ΔOD and change in phase $\Delta\phi$ upon photoexcitation at 800 nm.

Figure 7 displays the observed frequency-dependent ΔOD and $\Delta\phi$ when photoexciting at 800 nm. Both ΔOD and $\Delta\phi$ arise from changes of the conductivity in the LT-GaAs layer as well as the GaAs substrate. The data can be separated into two regimes: (1) Delay times from 0 to 1.3 ps pertain to the initial onset and rapid decay of conductivity, and are dominated by the response of carriers in LT-GaAs. (2) For delay times greater than 1.3 ps, the conductivity has essentially leveled off, and is due to the photoexcited carriers remaining in the GaAs substrate. The data obtained at 400 and 800 nm excitation (Figs. 2 and 7, respectively) are very different. Even though we are reporting the real and imaginary conductivity for the 400 nm data, and ΔOD and $\Delta\phi$ at 800 nm, we can in fact compare the trends in the two data sets because the ΔOD primarily reflects changes in the Re$[\sigma]$, and $\Delta\phi$ reflects changes in the Im$[\sigma]$.[20] With 400 nm excitation, Re$[\sigma]$ is frequency independent, however, with 800 nm excitation the ΔOD peaks at very low frequencies. The Im$[\sigma]$ rises up at the higher frequencies, and never shows a peak in our frequency range when photoexcited at 400 nm. On the other hand, $\Delta\phi$ shows a peak whose frequency changes as a function of pump-delay time with 800 nm excitation.

In order to model the measured ΔOD and $\Delta\phi$, we need to account for carriers in the LT-GaAs layer and GaAs substrate, as well as account for the interface between the photoexcited and non-photoexcited materials. To do so, we define a transmission amplitude ratio[17] for a dielectric stack consisting of several layers as shown here.

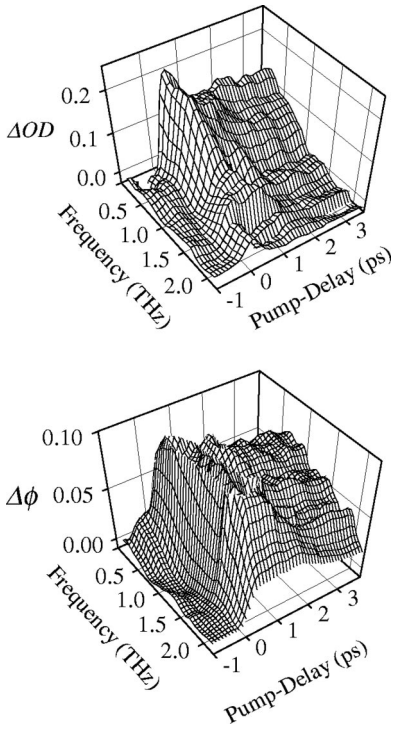

FIG. 7. Change in optical density (ΔOD) and change in phase ($\Delta\phi$) as a function of pump-delay time when photoexciting the LT-GaAs/GaAs structure at 800 nm.

5	4	3	2	1
Air	Photoexcited LT-GaAs 0.54 μm	LT-GaAs 0.46 μm	Photoexcited GaAs 0.70 μm	GaAs

This accounts for all of the interfaces encountered by the THz pulse as it propagates through the LT-GaAs/GaAs structure. The carrier spatial distributions are approximated as slab distributions, as already discussed in Appendix B of Ref. 17; the 0.54 μm layer thickness for photoexcited LT-GaAs was determined by normalizing the distribution of carriers in the LT-GaAs layer and then integrating. We have verified that this slab approximation is equivalent to the actual carrier distribution by performing FDTD calculations.[29]

A GCCD model is used for each of the two photoexcited layers, however, each layer will have unique values for ω_p, $\tau_{o,coll}$, and α. The LT-GaAs and GaAs values for ω_p are determined from the density of electrons in the appropriate layer. We parameterize the total density of excited carriers as a function of pump-delay time with an exponentially decreasing function with a long-time offset convoluted with a Gaussian function. Thus, $N_{tot}(t)$ is

$$N_{tot}(t) = N_o\{(1-b)\exp[(t-t_o)/\tau_l] + b\} \otimes G(t,t_o), \quad (2)$$

where N_o is the initial carrier density, b is the long-time offset, t_o is the arrival time of the visible pulse, $G(t,t_o)$ is a

Gaussian function centered at t_o with FWHM of Δw representing the visible pulse, and $\otimes$ represents a convolution.

The relative fractions of elections in LT-GaAs ($f_{\text{LT-GaAs}}$) and GaAs (f_{GaAs}) are known from the diffusion model, as shown in the inset of Fig. 5. The number of electrons in LT-GaAs and GaAs is related to the total number of excited carriers by $n_{\text{LT-GaAs}}=f_{\text{LT-GaAs}}n_{\text{tot}}$ and $n_{\text{GaAs}}=f_{\text{GaAs}}n_{\text{tot}}$, furthermore $n_{\text{tot}}=n_{\text{LT-GaAs}}+n_{\text{GaAs}}$. The density is related to the number of carriers n by $N=n/(Ad)$, where A is the area (spot size of laser), and d is the depth of the carrier distribution, A is the same value for the total, LT-GaAs, and GaAs distributions. Thus, one obtains the following two equations:

$$N_{\text{tot}}d_{\text{tot}}=N_{\text{GaAs}}d_{\text{GaAs}}+N_{\text{LT-GaAs}}d_{\text{LT-GaAs}}, \tag{3}$$

$$N_{\text{tot}}d_{\text{tot}}=f_{\text{GaAs}}N_{\text{tot}}d_{\text{tot}}+f_{\text{LT-GaAs}}N_{\text{tot}}d_{\text{tot}}. \tag{4}$$

The depth, d_{GaAs} for the carrier distribution in the GaAs substrate is the same as that of the total carrier distribution since both are exponential functions with the same $1/e$ value, therefore $d_{\text{GaAs}}=d_{\text{tot}}$. However, $d_{\text{LT-GaAs}}$ is shorter than d_{tot} by 23%, and thus $d_{\text{LT-GaAs}} = 0.77\ d_{\text{tot}}$. We arrive at the desired relationships: $N_{\text{GaAs}}=f_{\text{GaAs}}N_{\text{tot}}$ and $N_{\text{LT-GaAs}}=f_{\text{LT-GaAs}}N_{\text{tot}}/0.77$, so that $N_{\text{LT-GaAs}}$ and N_{GaAs} can be determined at each pump-delay time from Eqs. (2) to (4).

The scattering rate in GaAs is assumed to decrease as a function of pump delay, as was observed in a previous study of photoconductivity in regular GaAs.[3] We therefore parameterized $\tau_{\text{coll-GaAs}}$ with an exponential rise to a maximum function with time constant $\tau_{\tau,\text{coll-GaAs}}$, with an offset that increases from an initial value,$\tau_{\text{o,coll-GaAs}}$, to a long-time value. Thus, to fit the entire set of data (50 difference scans spaced 100 fs apart) we globally vary N_o, τ_l, t_o, b_N, $\alpha_{\text{LT-GaAs}}$, α_{GaAs}, $\tau_{\text{o,coll-GaAs}}$, and $\tau_{\tau,\text{coll-GaAs}}$, in a nonlinear least squares fitting routine, where α is the "Cole–Cole" parameter not the absorption coefficient. We vary $\tau_{\text{coll-LT-GaAs}}$ locally for each pump-delay time, keeping the global parameters fixed.

Figure 8 shows the observed data with the calculated data overlaid, and two representative cuts of the data are shown: one at 0.3 and the other at 1.5 ps following the 800 nm pump pulse. We see that the model fits the data quite well. A summary of the best fit parameters is given in Table I. The values for the mobility in GaAs agree well with our previously reported value for GaAs of 6540 $\text{cm}^2\ \text{V}^{-1}\ \text{s}^{-1}$ at carrier density of $1.6\times10^{16}\ \text{cm}^{-3}$.[3] The carrier lifetime τ_l is 1.4 ± 0.1 ps, and the FWHM of the Gaussian function is 250 fs. The offset, b_N, is $26\%\pm1\%$, which is smaller than that found for the 1D pump scan. This offset is for the carrier density and not the THz transmission, as in the 1D pump scans, and is close to the expected value of 23%. Figure 9 shows $\mu_{\text{LT-GaAs}}$ for all values of the pump-delay time, and it is seen that $\mu_{\text{LT-GaAs}}$ is essentially constant.

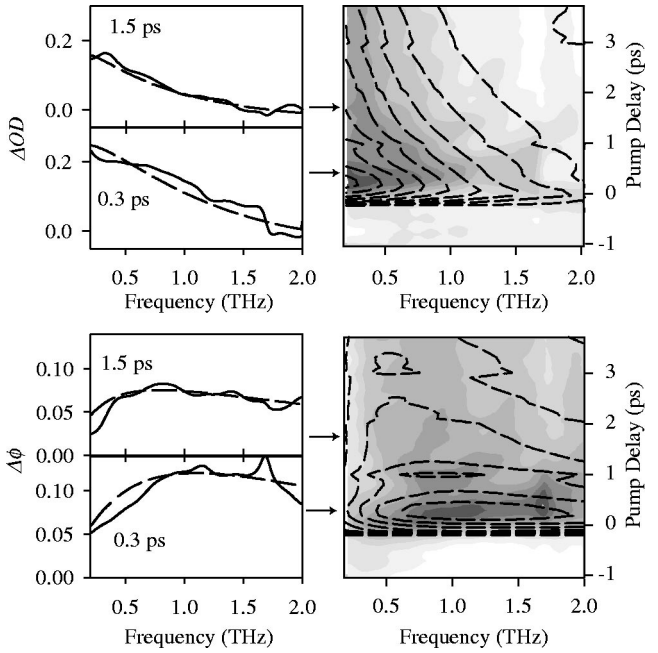

FIG. 8. Calculated ΔOD and $\Delta\phi$ compared to the measured data. The dashed lines are the calculated data and the shaded contours are the measured data shown in Fig. 7. Two cuts at 0.3 and 1.5 ps are shown on the left side. In the cuts the measured data are the solid lines, and the calculated data are the dashed lines. A color representation is available in the EPAPS repository (see Ref. 20).

IV. DISCUSSION

A. Lifetime vs mobility in LT-GaAs

Annealing the as-grown LT-GaAs material is known to increase both the static carrier mobility[30] and the carrier lifetime.[7] The static mobility of the as-grown material is between 1 and 3 $\text{cm}^2\ \text{V}^{-1}\ \text{s}^{-1}$, while that of an annealed sample is much higher and increases with anneal time and/or temperature.[30] The mobility in regular GaAs is $\sim$7000 $\text{cm}^2\ \text{V}^{-1}\ \text{s}^{-1}$ at 300 K.[3] During the annealing process the excess As atoms form clusters, reducing the lattice strain.[5] Increasing the anneal time and/or temperature results in larger clusters that have greater separation. Increasing the cluster separation results in longer carrier lifetimes,[7] while the decrease in lattice strain is responsible for an increase in mobility.

The reduced mobility of LT-GaAs compared to regular GaAs is due to residual shallow defects. Shallow defects are observed in LT-GaAs in the band-edge cw absorption spectrum,[31] and are not associated with midgap deep traps due to the As clusters. Figure 10 shows the band structure of LT-GaAs, differing only from GaAs by the presence of shallow defects and deep traps. The shallow defects reduce the mobility by increasing the scattering processes, and thereby

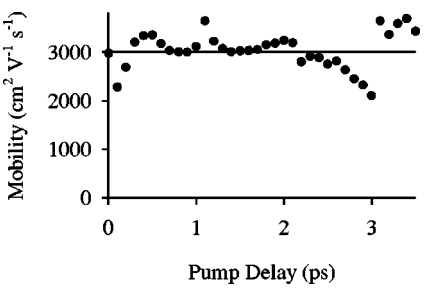

FIG. 9. Extracted values of the mobility in the LT-GaAs layer as a function of time after photoexciting at 800 nm.

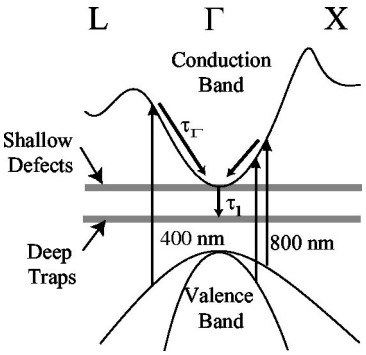

FIG. 10. The band structure of LT-GaAs is assumed in this study to be the same as that of GaAs, except that LT-GaAs has a band of shallow defects, and contains deep traps (associated with the As clusters). Relaxation of the photoexcited carriers initially occurs in the Γ valley with a time constant τ_Γ and then from the Γ valley into the midgap states with a time constant of τ_l. The shallow defects do not remove the electrons from the conduction band, but do decrease their mobility.

decreasing the time between collisions τ_{coll}, whereas the deep traps are responsible for the shorter lifetimes.

While the mobility in LT-GaAs is ~ 2 times smaller than in regular GaAs, it is still quite large. For example, silicon has a mobility of 1350 $\text{cm}^2\ \text{V}^{-1}\ \text{s}^{-1}$.[1] The carrier lifetime, on the other hand, is reduced by a factor of 10^3, from ~ 1 ns in regular GaAs (Ref. 3) to ~ 1 ps in LT-GaAs. While it is desirable, from a device standpoint, for a material to have high mobility with short carrier lifetime, there is a tradeoff between these traits in LT-GaAs materials; samples with higher mobility have longer carrier lifetimes.

In the general case of semiconductors, the carrier lifetime τ_l (which is on the order of nanoseconds) is not related to the mobility. This is because the mobility is related to the average carrier scattering time $\langle \tau_{\text{coll}} \rangle$, which is on the order of femtoseconds to picoseconds. The carrier lifetime τ_l is a measure of the interband dynamics, whereas $\langle \tau_{\text{coll}} \rangle$ is a measure of the intraband dynamics. However, the carrier lifetime in LT-GaAs and related semiconductor materials is governed by the average time a photoexcited carrier diffuses before encountering a trap, and this diffusion time is determined by the mobility. Thus, there is a phenomenological relationship between the carrier lifetime and the mobility through the anneal conditions. The mobility is related to the anneal conditions through the reduced lattice strain, but the carrier lifetime is related to the anneal conditions through the As cluster separation.

To be quantitative, we treat the carriers as diffusing particles undergoing Brownian motion which can be described by Maxwell–Boltzmann statistics. Then, the average distance a particle diffuses in time t is $\langle x \rangle = \sqrt{Dt}$,[21] where D is the diffusion coefficient. The mobility is related to D through the Einstein relation, $D = \mu k_{\text{B}} T/e$, where k_{B} is the Boltzmann constant, T is the temperature, and e is the charge of an electron. Since the carrier lifetime is the average time that the carriers diffuse before encountering an As cluster, the mobility can be related to the carrier lifetime by

$$\mu = \frac{\langle x \rangle^2 e}{\tau_l k_B T}, \tag{5}$$

where $\langle x \rangle$ is the average distance between clusters, and τ_l is the lifetime of the carriers. From this relationship the mobility is seen to be inversely related to the carrier lifetime τ_l as expected. Using a mobility of 3000 $\text{cm}^2\ \text{V}^{-1}\ \text{s}^{-1}$ and a temperature of 300 K, we calculate a cluster separation of ~ 960 Å . This distance is somewhat larger than those reported in Ref. 7 for the same carrier lifetime. However, the anneal time for their sample was only 30 s while our sample was annealed for 30 min, thus achieving a higher mobility and larger cluster separation.

B. Time-dependent mobility

Carriers are photoexcited into the conduction band with excess energy. The excess energy initially is deposited into the carrier kinetic energy resulting in elevated carrier temperatures. If the excitation energy is above that of the L and/or X valley minima, then intervalley scattering occurs on the 10–100 fs time scale. Intervalley scattering proceeds via emission of large wave-vector phonons[32] which must decay through multiphonon processes. The excited carriers within the Γ valley also relax by emitting phonons, of which the largest contribution is that of the LO phonons. In this way, the carriers transfer energy to the lattice and eventually achieve thermodynamic equilibrium. Due to rapid intervalley scattering and large excess energies associated with 400 nm excitation, a large nonequilibrium population of ''hot'' phonons is produced. In this situation, the carriers may emit or absorb phonons with roughly equal probability, and the carriers cannot relax until the hot phonon population relaxes, which occurs with a time constant of 1–4 ps.[32–36] Thus, the hot phonons effectively slow down the thermalization time of the carriers.

We observe a time-dependent increase of μ from 400 ± 100–$1100 \pm 100 \text{cm}^2\ \text{V}^{-1}\ \text{s}^{-1}$ with a time constant of 2.0 ps (Fig. 4) when photoexciting at 400 nm. The mobility increases as the number of scattering events decreases. A time constant of 2.0 ps is in qualitative agreement with the relaxation time within in the Γ valley obtained from the three-state model proposed by Stanton and Bailey,[19] which was used to fit the onset of photoconductivity when photoexciting into the L or X valleys (Fig. 1). The relaxation in the Γ valley determined from that model was 2 ± 1 ps.

It has recently been shown that the presence of hot phonons can affect the measured free carrier absorption (FCA) because FCA is a phonon-mediated process.[36,37] That is, to conserve both energy and momentum, intraband absorption must be accompanied by either absorption or emission of a phonon. This is the reason why FCA measurements can be related to the mobility. In Ref. 36 hot phonons were seen to increase the measured FCA where the photon energy used was 73 meV, about two times larger than the 36 meV LO phonon energy. However, in the work reported here, the probe photon energies used are 1–10 meV and the excess hot phonons are seen to decrease the FCA. One might expect the additional phonons to increase the magnitude of FCA because there are more of them available to assist in the absorption, but more phonons lead to a higher scattering rate and therefore a lower mobility. It is well known that at high

frequencies $\omega\langle\tau_{\text{coll}}\rangle \gg 1$ the mobility is *inversely* proportional to the FCA,[38] however, at low frequencies FCA is *directly* proportional to the mobility. Free-carrier absorption can be described quantum mechanically as a three-particle interaction (electron, photon, phonon) using second order time-dependent perturbation theory.[39] It has been shown that the Drude model reproduces the quantum mechanical results in the low frequency limit ($\hbar\omega < k_B T$) when the scattering is elastic.[40–42] The Drude model makes no assumptions as to the nature of the scattering processes and will reflect the presence of excess phonons by a decrease in the mobility. The Drude model predicts that a decrease in mobility leads to a decrease in the absorption at low frequencies as observed by us, but an increase in the absorption at high frequencies as observed in Ref. 36.

LT-GaAs has a larger mobility when the carriers are excited with 800 nm light than with 400 nm light, and furthermore, the mobility is time-independent when excited at 800 nm. Photoexcitation at 400 nm produces carriers with 1.67 eV excess energy, whereas photoexcitation at 800 nm produces carriers with only 0.12 eV excess energy. The temperature of the carriers when excited at 400 nm is higher than when photoexcited at 800 nm. Phenomenologically, we see from Eq. (5) that a high carrier temperature results in a lower mobility even though the carriers have a higher kinetic energy. We expect the mobility to be reduced when exciting at 400 nm because of the large population of phonons produced. The carrier lifetime is essentially the same for both 400 and 800 nm excitation, even though the mobilities are quite different, because T is different. In addition to their excess energy, photoexcitation at 400 nm creates carriers with larger effective mass, due to the combined effects of carriers in the low mobility L and X valleys as well as being higher up in the Γ valley, where the curvature is lower. Additionally, the 400 nm excitation creates a larger density of carriers than photoexcitation at 800 nm, even with the same number of excited carriers because the optical skin depth is 50 times smaller. Higher densities result in lower mobilities[3] due to increased carrier–carrier interactions.

C. Conductivity measurements using TRTS

Time-resolved THz spectroscopy measurements are most sensitive to peak frequencies ranging from 0.1 to 2.9 THz, corresponding to scattering times between $\tau_{\text{coll}} = 1/(0.1\times 2\pi) = 1.6$ ps and $1/(2.9\times 2\pi) = 56$ fs, respectively. For a symmetric log distribution of relaxation times, as obtained with the "Cole–Cole" modification of the Drude model, the peak of $\text{Im}[\sigma]$ occurs at $\omega = 1/\langle\tau_{\text{coll}}\rangle$, or a linear frequency of $\nu = 1/(2\pi\langle\tau_{\text{coll}}\rangle)$. As $\langle\tau_{\text{coll}}\rangle$ becomes smaller or larger, the peak will move out of our frequency window. For nonsymmetric distributions the peak does not occur precisely at $1/(2\pi\langle\tau_{\text{coll}}\rangle)$ but shows the same general trend. For LT-GaAs photoexcited at 400 nm, $\langle\tau_{\text{coll}}\rangle$ is between 10 and 50 fs, which results in a peak in the $\text{Im}[\sigma]$ between 3.3 and 17 THz, which is outside our frequency range. This is the reason that the measured frequency-dependent complex conductivity in Fig. 2 shows essentially no curvature. For the extreme case when $\langle\tau_{\text{coll}}\rangle \ll 56$ fs, the $\text{Im}[\sigma]$ would show essentially no response, but the $\text{Re}[\sigma]$ would have a constant value, corresponding to a change in absorption with no change in index of refraction. At the other extreme, when $\langle\tau_{\text{coll}}\rangle \gg 1.6$ ps, neither the $\text{Im}[\sigma]$ nor $\text{Re}[\sigma]$ would be measurable.

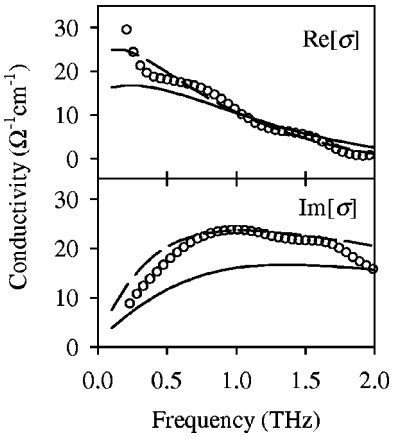

FIG. 11. Comparison of the two different ways to add conductivities with the measured effective conductivity in the LT-GaAs/GaAs structure. The circles are the effective conductivity, the solid lines are obtained when the scattering rates are averaged, and the dashed lines correspond to adding the conductivities. The data are from 0.5 ps after photoexcitation with 800 nm light.

The results in Sec. III allow important general observations to be made about conductivity measurements using TRTS. Consider photoexcitation of the LT-GaAs/GaAs sample at 800 nm, in which the THz probe pulse encounters two different types of absorbers; photoexcited carriers in LT-GaAs and those in GaAs. If we did not know *a priori* what the underlying distribution of materials was, we would only be aware of an *effective* photoconductivity for the composite sample. That effective conductivity could arise from two different ways of combining the individual conductivities. It could be the sum of the individual conductivities, $\sigma_{\text{tot}} = \Sigma\sigma_i$, or it could arise from an average of their scattering times, $\sigma_{\text{tot}} = \sigma(\langle\tau_{\text{coll}}\rangle)$, where $1/\langle\tau_{\text{coll}}\rangle = \Sigma a_i/\tau_{\text{coll},i}$, and a_i is the fraction of carriers having $\tau_{\text{coll},i}$. We obtain different results from these two cases.

As an example, Fig. 11 compares these two ways of combining individual conductivities to the observed results. We use the best fit parameters when photoexcited at 800 nm to calculate the conductivity of GaAs and LT-GaAs at a pump-delay time of 0.5 ps, and then added them together (shown as the dashed lines in Fig. 11). We then calculated the average scattering time from the individual scattering times and calculated the resulting conductivity (shown with the solid lines). We obtained the *effective* conductivity from the measured ΔE_{THz} as described in Appendix B of Ref. 17, and it is shown with open circles. It is seen that adding the individual conductivities more correctly reproduces the measured data than averaging the scattering times. This is expected because it is known that our sample consists of two separate layers.

The situation is different when the same carrier can undergo a variety of scattering processes, and the overall scattering time is given by

$$\frac{1}{\tau_{\text{coll,tot}}} = \sum_i \frac{a_i}{\tau_{\text{coll},i}}, \tag{6}$$

where a_i is the appropriate weight for the ith scattering time, assuming the scattering times are within the range mentioned above. This occurs, for example, in confined systems such as quantum dots. For these systems there are two classes of conduction for the electrons; conduction within the nanoparticle and conduction between the particles. The transport between nanoparticles proceeds via a hopping mechanism, and results in very long hopping times (very high effective scattering rates), which are too long to be measured with our current sensitivity. However, the conductivity within each individual nanoparticle will lead to THz absorption. In cases such as these we expect very different results for the conductivity when measured with TRTS compared to a dc transport method. dc measurements of the long range transport are limited by the interparticle conductivity, whereas TRTS measures intraparticle conductivity. Furthermore, dc or long range transport measurements are limited to measuring the drift conductivity σ_{drift}, which is given by $1/\sigma_{\text{drift}} = 1/\sigma_+ + 1/\sigma_-$, where $\sigma_\pm$ denotes the hole/electron conductivity. The electrons (or holes) may be quite mobile locally, but cannot diffuse large distances because of Coulombic attractions to the positive (negative) charges. TRTS measurements are sensitive to the localized conductivity, and are also influenced by the effective mass of the carriers. We will be able to study the size dependent conductivity and observe the effects of quantum confinement on the conduction electrons using TRTS.

V. CONCLUSIONS

We find that the mobility of photoexcited electrons in LT-GaAs is lower than in regular GaAs, and attribute the reduction to residual defects and strain from the excess As. We find that the carriers relax in the Γ valley with a time constant of 1–2 ps when photoexciting at 400 nm, and that the mobility increases as the carriers relax. Also, the carrier lifetime is determined to be 1.1 ± 0.1 ps, and we have given a phenomenological relationship that can be used to estimate the mobility based on knowledge of the carrier lifetime in LT-GaAs materials.

We have also argued that TRTS can be used to study the localized conductivity rather than long range transport. This makes TRTS a powerful tool for studying systems which are difficult to study by conventional methods. In particular, study of the conductivity in nanoparticles will greatly benefit from this method because it is a localized noncontact probe, and we are currently pursuing such studies.

ACKNOWLEDGMENTS

The authors acknowledge the National Science Foundation and Sloan Foundation for partial support of this work.

[1] J. I. Pankove, *Optical Processes in Semiconductors* (Prentice-Hall, Englewood Cliffs, NJ, 1971).
[2] S. E. Ralph, Y. Chen, J. Woodall, and D. McInturff, Phys. Rev. B **54**, 5568 (1996).
[3] M. C. Beard, G. M. Turner, and C. A. Schmuttenmaer, Phys. Rev. B **62**, 15764 (2000).
[4] J. Linnros, J. Appl. Phys. **84**, 275 (1998).
[5] M. Melloch, J. Woodall, E. Harmon, N. Otsuka, F. Pollak, D. Nolte, R. Feenstra, and M. Lutz, Annu. Rev. Mater. Sci. **25**, 547 (1995).
[6] H. Wang and J. Whitaker, J. Electron. Mater. **22**, 1461 (1993).
[7] E. Harmon, M. Melloch, J. Woodall, D. Nolte, N. Otsuka, and C. Chang, Appl. Phys. Lett. **63**, 2248 (1993).
[8] Z. Liliental-Weber, H. Cheng, S. Gupta, J. Whitaker, K. Nichols, and F. Smith, J. Electron. Mater. **22**, 1465 (1993).
[9] D. You, R. R. Jones, P. H. Bucksbaum, and D. R. Dykaar, Opt. Lett. **18**, 290 (1993).
[10] A. Rice, Y. Jin, X. F. Ma, X. C. Zhang, D. Bliss, J. Larkin, and M. Alexander, Appl. Phys. Lett. **64**, 1324 (1994).
[11] Q. Wu, M. Litz, and X. C. Zhang, Appl. Phys. Lett. **68**, 2924 (1996).
[12] A. Nahata, A. S. Weling, and T. F. Heinz, Appl. Phys. Lett. **69**, 2321 (1996).
[13] G. Gallot, J. Q. Zhang, R.W. McGowan, T. I. Jeon, and D. Grischkowsky, Appl. Phys. Lett. **74**, 3450 (1999).
[14] G. Gallot and D. Grischkowsky, J. Opt. Soc. Am. B **16**, 1204 (1999).
[15] H. J. Bakker, G. C. Cho, H. Kurz, Q. Wu, and X. C. Zhang, J. Opt. Soc. Am. B **15**, 1795 (1998).
[16] D. Aspnes and A. A. Studna, Phys. Rev. B **27**, 985 (1982).
[17] See EPAPS Document No. E-JAPIAU-90-069124 for additional details about the collection and analysis of data in TRTS experiments. This document may be retrieved via the EPAPS homepage (http://www.aip.org/pubservs/epaps.html) or from ftp.aip.org in the directory /epaps/; see the EPAPS homepage for more information.
[18] *Landolt-Börnstein*, edited by K.-H. Hellwege and O. Madelung, Vol. 17a Semicondutors, Physics of Group IV Elements and III-V Compounds, (Springer-Verlag, New York, 1982).
[19] C. J. Stanton and D. W. Bailey, Phys. Rev. B **45**, 8369 (1992).
[20] See EPAPS Document No. E-JAPIAU-90-069124 for a color version of Fig. 2 that also includes a comparison to ΔOD and $\Delta\phi$, as well as color versions of Figs. 3 and 8. This document may be retrieved via the EPAPS homepage (http://www.aip.org/pubservs/epaps.html) or from ftp.aip.org in the directory /epaps/; see the EPAPS homepage for more information.
[21] N. Ashcroft and N. Mermin, *Solid State Physics* (Saunders College Publishing, New York, 1976).
[22] E. Abramof and A. da Silva, Phys. Rev. B **55**, 9584 (1997).
[23] K. S. Cole and R. H. Cole, J. Chem. Phys. **9**, 341 (1941).
[24] T. I. Jeon and D. Grischkowsky, Phys. Rev. Lett. **78**, 1106 (1997).
[25] T. I. Jeon and D. Grischkowsky, Appl. Phys. Lett. **72**, 2259 (1998).
[26] C. Böttcher and P. Bordewijk, *Theory of Electric Polarization*, 2nd ed. (Elsevier, New York, 1978), Vol. 2.
[27] W. H. Press, S. A. Teukolsky, W. T. Vetterling, and B. P. Flannery, *Numerical Recipes in Fortran*, 2nd ed. (Cambridge University Press, New York, 1986).
[28] D. McQuarrie, *Statistical Mechanics* (Harper Collins, New York, 1976).
[29] M. C. Beard and C. A. Schmuttenmaer, J. Chem. Phys. **114**, 2903 (2001).
[30] N. Atique, E. Harmon, J. Chang, J. Woodall, M. Melloch, and N. Otsuka, J. Appl. Phys. **77**, 1471 (1995).
[31] G. Segschneider, T. Dekorsy, H. Kurz, R. Hey, and K. Ploog, Appl. Phys. Lett. **71**, 2779 (1997).
[32] A. Othonos, Appl. Phys. Lett. **83**, 1789 (1998).
[33] P. Langot, N. Del Fatti, D. Christofilos, R. Tommasi, and F. Valleé, Phys. Rev. B **54**, 14487 (1996).
[34] H. van Driel, Phys. Rev. B **19**, 5928 (1979).
[35] J. Shah, *Ultrafast Spectroscopy of Semiconductors and Semiconductor Nanostructures* (Springer, New York, 1999).
[36] H. P. M. Pellemans and P. C. M. Planken, Phys. Rev. B **57**, R4222 (1998).
[37] P. Yu and M. Cardona, *Fundamentals of Semiconductors: Physics and Materials Properties* (Springer, Berlin, 1996).
[38] P. Butcher and D. Cotter, *The Elements of Nonlinear Optics* (Cambridge University Press, Cambridge, 1990).
[39] B. Jensen, Ann. Phys. (N.Y.) **80**, 284 (1973).
[40] B. Jensen, Ann. Phys. (N.Y.) **95**, 229 (1975).
[41] B. Jensen, Solid State Commun. **24**, 853 (1977).
[42] B. Jensen, J. Appl. Phys. **50**, 5800 (1979).

Supplementary information for: Sub-picosecond carrier dynamics in low-temperature grown GaAs as measured by time-resolved THz spectroscopy

Matthew C. Beard, Gordon M. Turner, and Charles A. Schmuttenmaer
Chemistry Department, Yale University, 225 Prospect St., P.O. Box 208107, New Haven, CT 06520-8107

(Dated: December 2001)

I. INTRODUCTION

The following information is archived in the Electronic Physics Auxiliary Publication Service (EPAPS), and is provided as supplementary material to Ref. 1. As time-resolved THz experiments become more widely used, it is essential that the measured data is treated correctly to obtain accurate results. The following two appendices provide information that is crucial to the correct collection and analysis of data in time-resolved terahertz spectroscopic (TRTS) studies. Appendix A deals with how to collect a complete two-dimensional (2D) data set and deconvolve the detector response. Appendix B describes the procedure for extracting the far-infrared optical constants of a photoexcited medium from the measured change in terahertz transmission.

APPENDIX A: DATA ACQUISITION AND DETECTOR DECONVOLUTION

We have shown previously[2] that a full two dimensional (2D) grid of THz difference scans $\Delta E_{\mathrm{THz}}(t, t'')$, corresponding to pump on minus pump off, is needed when the response of the material is fast compared to the temporal duration of the THz pulse, where t is the THz-delay time and t'' marks the arrival of the pump pulse. For most samples this is only important near $t'' = 0$, when the pump arrives during the propagation of the THz pulse. Consider Fig. 1, which displays a 2D TRTS data set, where a series of THz difference scans are taken at a variety of pump-delay intervals. It is clear from Fig. 1 that the individual THz difference scans are strongly influenced by the arrival of the pump pulse (shown as arrows). In Refs. 2 and 3 we show that the data parallel to the 45° axis of this plot (shown with a bold line) consist of THz difference scans which have experienced a constant delay from the pump pulse. These scans can be obtained by a numerical projection of the original data set, scanning the THz transmitter delay in reverse, or equivalently, synchronously scanning the THz receiver and pump delay together with fixed THz transmitter delay. Any of these methods will result in a data set which is comprised of THz scans that have experienced a constant delay from the pump pulse.

Figure 2(a) displays a data set for GaAs which has been collected in this manner. We immediately notice two features: the 45° component in Fig. 1 is not present, and a new component curving to the left at early pump-delay times has appeared. This new feature and appears to grow in *before* the arrival of the pump pulse. This apparent superluminal phenomenon is easily understood from the convolution of the true THz waveform with the detector response function, yet this effect has not been noted previously.

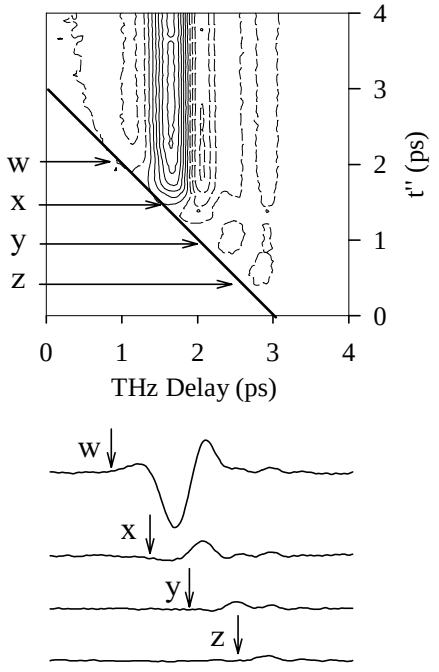

FIG. 1: Typical TRTS 2D data set. Contour plot of ΔE_{THz} (pump on minus pump off). The solid lines are negative values and the dashed lines are positive. The bold solid diagonal line represents the arrival of the pump pulse. The pump pulse affects only that part of the THz pulse which comes after it. Below are individual scans corresponding to the arrows on the grid, the arrows represent the arrival of the visible pulse.

Consider Fig. 3 (a), in which a hypothetical reference pulse is shown (solid line) after passing through the sample, but before propagating through the ZnTe detector crystal. Overlaid is a pulse that has experienced photoexcitation while the THz pulse was in the sample (dashed

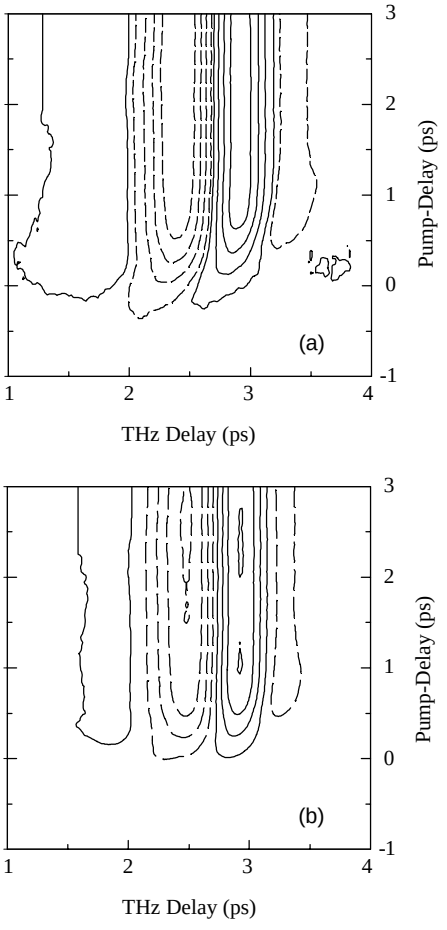

FIG. 2: (a) Contour plot of ΔE_{THz}(pump-on minus pump-off) as a function of constant reference time. The solid lines correspond to positive ΔE_{THz} values and the dashed lines correspond to negative values. The 45° component seen in Fig. 1 has been removed as explained in the text. However, there is a component near pump-delay $t'' = 0$ which curves to the left and appears to come before the pump pulse has arrived. (b) After deconvolution these features have essentially been removed.

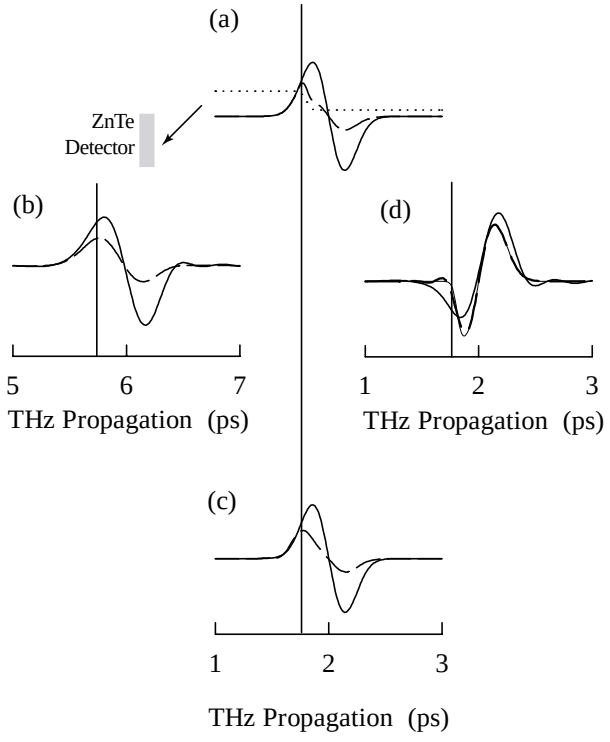

FIG. 3: Illustration of the detector filtering effect on a THz pulse transmitted through a photoexcited medium. In (a), the solid line is the reference scan (no photoexcitation), the dashed line represents the transmitted pulse when there is photoexcitation, and the dotted line represents a decrease in sample transmission due to the photoexcitation pulse. The reference and photoexcited pulses are identical until the moment of photoexcitation, represented by the vertical line. (b) Propagation through the detector (ZnTe) distorts the waveforms. (c) Numerical deconvolution of the detector response removes the effect of propagation and nearly restores the scans to their shape prior to propagation. The *differences* between the reference and photoexcited scans are shown in (d) to further illustrate this point. The thin solid line is the difference before propagation, the bold solid line is the difference after propagation and without deconvolution, and the dashed line (hardly distinguishable from the thin solid line) is the difference after deconvolution.

line), such that only the trailing portion of the pulse is affected by the photoexcitation (the vertical line indicates the moment of photoexcitation). After propagation through the detector, the photoexcited output pulse [Fig. 3 (b)] has features that appear to differ from the reference pulse *before* the pump pulse arrives. This is because the finite-bandwidth of the detector acts as a low-pass filter, broadening the true pulse. To correct for this artifact we deconvolve the detector response from the measured signal. After deconvolution, the reference and the photoexcited scans [Fig. 3 (c)] are largely restored to their shapes before convolution with the detector response, and the features occurring before the arrival of the pump pulse have essentially disappeared.

To perform the detector deconvolution we use a Fourier transform method including optimal filtering.[4] The electro-optic detection of a THz pulse has been modelled by Bakker *et al.*[5] and is given by

$$\Delta I_{\mathrm{EO}}(\tau) \propto r_{41} \int_0^l dz \int_{-\infty}^{\infty} dt I_p(z, t-\tau) E(z,t) \quad \text{(A1)}$$

with

$$E(z,t) = \int_{-\infty}^{\infty} d\omega E(0,\omega) \exp(izk_{\mathrm{ZnTe}} - i\omega t), \quad \text{(A2)}$$

where $\Delta I_{\mathrm{EO}}(\tau)$ is the detected signal, $E(z,t)$ is the propagated THz pulse at a distance z into the detector crystal, $I_p(z, t-\tau)$ represents the propagating visible pulse (taken as Gaussian), and τ is the temporal delay between the two pulses, k_{ZnTe} is the complex propagation vector of the THz pulse in the ZnTe crystal, and r_{41} is the electro-optic coefficient for ZnTe. To obtain the THz pulse before

propagation through the detector, $E(0,t)$, we can regard Eq. (A1) as a simple convolution of the detector response with the THz pulse given by

$$\Delta I_{\mathrm{EO}}(\tau) \propto \int_{-\infty}^{t} E(0,t)\chi_d(t-\tau)dt, \qquad \text{(A3)}$$

with χ_d being the response function of the detector. If χ_d is known, a Fourier deconvolution can be used to obtain $E(0,t)$. The detector response function, χ_d, is most easily generated by numerically propagating a Dirac delta function through the detector using Eqs. (A1) and (A2). The complex propagation vector is $k_{\mathrm{ZnTe}} = \omega n(\omega)/c + i\omega\alpha(\omega)/(2c)$, where $n(\omega)$ and $\alpha(\omega)$ are the index of refraction and absorption coefficient for ZnTe in the FIR, as measured in a separate THz-TDS measurement from 0.2 to 2.5 THz. Literature values were used to extended the FIR coverage to about 10 THz.[6]

The deconvolution procedure requires collecting the data in the conventional fashion as shown in Fig. 1: the pump-delay line is fixed while scanning the THz (probe) delay line. Each THz difference scan is then deconvolved from the detector. Finally, the data are numerically projected to obtain deconvolved difference scans with constant pump-delay times. The effect of convolution with the detector is largely removed by this process, as seen in Fig. 2 (b). Once the data have been correctly deconvolved and numerically projected, the frequency-dependent optical parameters can be extracted as discussed in Appendix B.

When the response of the material is slow compared to the detector response time, deconvolution is not required. For example, Fig. 4 is a 2D plot of the response of LT-GaAs, photoexcited at 400 nm, collected when scanning the THz transmitter in reverse. Photoexcitation at 400 nm produces electrons that immediately (∼10 fs) scatter to the low mobility L and X valleys. The FIR response is then governed by the return of the electrons to the high mobility Γ valley.[2,7–9] As a result, the rise time of the THz absorption is much slower and deconvolution is not required. Figure 4 shows the collected data without deconvolution, and there are no artifacts visible.

The group velocity mismatch of the pump and probe pulses can be neglected, since they traverse less than 2 microns of photoexcited material. The temporal resolution of TRTS is determined by the ∼ 200 fs detector response function and any geometrical limitations such as spatial overlap of the pump and probe beams, or non-collinear propagation of the beams.[2]

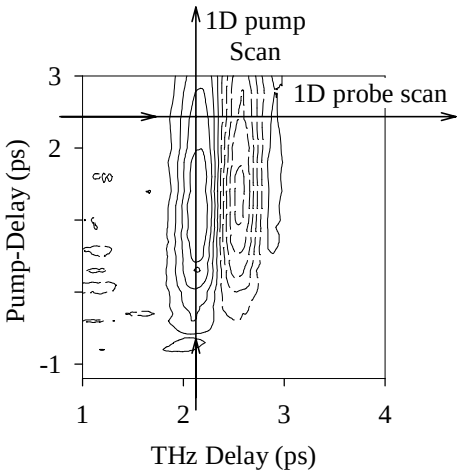

FIG. 4: Contour plot of THz difference scan of LT-GaAs photoexcited at 400 nm, solid lines are negative values and dashed lines correspond to positive values. The FIR response is slower when photoexcitation occurs at 400 nm compared to 800 nm, therefore, there is no need for detector deconvolution. One dimensional cuts can be taken from the data: 1D pump scans are parallel to the pump-delay axis and 1D probe scans are parallel to the THz-delay axis.

APPENDIX B: DATA ANALYSIS

Taking cuts of the 2D grid allows us to analyze the average dynamics measured in the experiment. A cut parallel to the pump-delay axis is a 1D pump scan (see Fig. 4), and a cut parallel to the THz-delay axis is a 1D probe scan. The 1D pump scans give the average THz absorption as a function of pump-delay time. By Fourier transforming the 1D probe scans, we obtain the frequency-dependent optical constants of the photoexcited material at some point in time after photoexcitation. We can obtain these 1D cuts experimentally by fixing the THz-delay and scanning the pump-delay (1D pump scan), or fixing the pump-delay and scanning the THz-delay (1D probe scan). We collect the 2D grid by collecting a series of 1D probe scans at a variety of pump-delay times.

Many systems studied with TRTS can be thought of as layered stacks of dielectric materials. In the case of a photoexcited semiconductor whose optical skin depth is less than its own thickness, the dielectric stack consists of semi-infinite layers of air that surround finite layers of photoexcited and nonphotoexcited semiconductor. The frequency-dependent index of refraction $n_{\mathrm{p}}(\omega)$ and absorption coefficient $\alpha_{\mathrm{p}}(\omega)$ of the photoexcited sample can be extracted from the measured data without assuming a model to describe the medium. To extract $n_{\mathrm{p}}(\omega)$ and $\alpha_{\mathrm{p}}(\omega)$ we must know the photoexcited path length d, and be able to describe the reflectivity losses at all the interfaces, which are not known *a priori*. Furthermore, the photoexcited/non-photoexcited interface is not well defined because the photoexcited medium gradually transforms into the non-photoexcited medium. The photoexcited path length d is usually small compared to the spatial extent of the THz pulse. This can result in interface effects that cause apparent superluminal propagation through photoexcited materials.[10] If not treated correctly, these interface effects, which are most pronounced when there are large changes in $n(\omega)$, can lead to large

errors in determining the optical properties.

Photoexcitation creates an exponentially decreasing distribution of carriers as a function of distance into the sample. The spatial distribution of carriers evolves as a function of time as the excited carriers diffuse, recombine at the surface, and/or undergo bulk recombination. These effects can be modelled to determine the carrier spatial distribution at any given pump-delay time.[2] For most cases, diffusion is only important at longer pump-delay times when $t > d_\circ^2/D$, where D is the diffusion coefficient and $d_\circ$ is the initial photoexcited path length. In a first approximation, we treat the photoexcited distribution as a uniform slab with thickness d. We choose d such that the volume of the assumed slab distribution is the same as the actual distribution, which is the $1/e$ point for an exponential distribution, referred to as the optical skin depth. In the case of non-exponential distributions, the slab thickness is determined by normalizing the distribution such that its maximum is unity. The integral of the normalized distribution is the appropriate thickness, d. To understand conditions under which the slab approximation holds, we have performed finite-difference time-domain (FDTD) simulations of TRTS experiments[11] using different non-uniform spatial distributions. It is found that the slab approximation is valid as long as the spatial extent of the distribution is less than ~ 5 μm.

In a TRTS experiment, we measure a complex ratio of the THz field with pump on (photoexcited) vs pump off (non-photoexcited):

$$\theta_{\rm meas} = E_{\rm p}^*(\omega, d)/E_{\rm np}(\omega, d), \tag{B1}$$

where $E_{\rm p}^*(\omega, d)$ is the complex field measured after transmission through the photoexcited material, and $E_{\rm np}(\omega, d)$ is the field measured after transmission through the non-photoexcited material. Since this work is done in the time domain, the THz difference pulse $\Delta E(t, d) = E_{\rm p}^*(t, d) - E_{\rm np}(t, d)$ is measured and combined with $E_{\rm np}(t, d)$ to yield $E_{\rm p}^*(t, d)$. Each are Fourier transformed to give $E_{\rm np}(\omega, d)$ and $E_{\rm p}^*(\omega, d)$ which then yields $\theta_{\rm meas}$.

Treating the interfaces in the dielectric stack is accomplished by relating $\theta_{\rm meas}$ to a complex transmission amplitude coefficient $\zeta(k)$, which accounts for the reflectivity of each interface, as well as propagation through the structure. The transmission coefficient relates the complex transmitted electric field amplitude $\mathcal{E}_{\rm tr}(\omega, d)$ to the complex initial electric field amplitude[12] $\mathcal{E}_\circ(\omega, 0)$ as

$$\mathcal{E}_{\rm tr}(\omega, d) = \zeta(k)\mathcal{E}_\circ(\omega, 0). \tag{B2}$$

In general, $E = \mathcal{E}\exp(ikz - i\omega t)$ where E is the full complex electric field, $\mathcal{E}$ is the complex amplitude, and k is the complex wave vector given by

$$k(\omega) = \frac{2\pi n(\omega)}{\lambda} + i\frac{\alpha(\omega)}{2}. \tag{B3}$$

The transmission coefficient is further defined in terms of the impedances of each layer in the stack by[12]

$$\frac{1}{\zeta(k)} = \prod_{j=1}^{j=n-1} \frac{Z_{j+1} + Z_{\rm in}^{(j)}}{Z_j + Z_{\rm in}^{(j)}} \exp(-i\phi_j), \tag{B4}$$

where $\zeta(k)$ is the transmission coefficient for a wave incident on layer n of an n-layered stack, and $\phi_j = k_j(\omega)d_j$. The propagation distance through the $j^{\rm th}$ layer d_j is defined as zero for the semi-infinite end layers of $j = 1$ and $j = n$. The impedance of the $j^{\rm th}$ layer is defined as $Z_j = \omega/ck_j(\omega)$, and the input impedance of the $j^{\rm th}$ interface is defined as

$$Z_{\rm in}^{(j)} = \frac{Z_{\rm in}^{j-1} - iZ_j\tan\phi_j}{Z_j - iZ_{\rm in}^{j-1}\tan\phi_j} Z_j, \tag{B5}$$

where $Z_{\rm in}^{(0)} = Z_1$.

The FIR optical properties of the photoexcited material are related directly to $\theta_{\rm meas}$ via the complex transmission amplitude coefficients of the photoexcited $\zeta_{\rm p}^*(k_{\rm p}^*)$ and non-photoexcited $\zeta_{\rm np}(k_{\rm np})$ media. From the definition of $\zeta(k)$ in Eq. (B2),

$$\theta_{\rm meas} = \frac{\zeta_{\rm p}^*(k_{\rm p}^*)}{\zeta_{\rm np}(k_{\rm np})}. \tag{B6}$$

The non-photoexcited transmission coefficient $\zeta_{\rm np}(k_{\rm np})$ can be obtained through a separate non-time-resolved measurement of the FIR optical properties of the material. By inverting Eq. (B6) we can obtain $k_{\rm p}^*$, the wave vector for the photoexcited medium and thus, $\alpha_{\rm p}(\omega)$ and $n_{\rm p}(\omega)$, the photoexcited optical constants. For this study, we do the inversion numerically by generating a grid of $|\theta(\alpha_{\rm guess}, n_{\rm guess}) - \theta_{\rm meas}|$ and finding the minimum on the grid, but other numerical procedures for solving these equations, such as the Newton-Raphson method, have been employed as well. By successively narrowing the grid we obtain values for $\alpha_{\rm p}(\omega)$ and $n_{\rm p}(\omega)$ whose accuracy are not limited by this numerical procedure.

The complex permittivity $\varepsilon = \varepsilon' + i\varepsilon''$ is determined from $\alpha_{\rm p}$ and $n_{\rm p}$ using $\varepsilon' = n_{\rm p}^2 - [\alpha c/(2\omega)]^2$ and $\varepsilon'' = n_{\rm p}\alpha_{\rm p}c/\omega$. The complex conductivity is obtained from

$$\varepsilon = \varepsilon_{\rm bound} - \left(\frac{i\sigma}{\varepsilon_\circ\omega}\right), \tag{B7}$$

where $\varepsilon_{\rm bound}$ is the part of the permittivity due to the non-photoexcited material, and $\varepsilon_\circ$ is the permittivity of free space.

It is worth noting that this procedure for extracting the photoexcited optical constants of a single layer in the dielectric stack assumes that none of the other layers' optical constants change upon photoexcitation. When multiple layers are excited, it is mathematically impossible to determine all of the individual optical constants. However, even in these cases, TRTS still measures the changes in optical density and phase of the complete stack, but extraction of material parameters for each layer depends on additional information about the system. This situation is exemplified in the study of photoexcitation of LT-GaAs at 800 nm.[1]

REFERENCES

[1] M. C. Beard, G. M. Turner, and C. A. Schmuttenmaer, J. Appl. Phys. **90**(12) (2001).

[2] M. C. Beard, G. M. Turner, and C. A. Schmuttenmaer, Phys. Rev. B **62**, 15764 (2000).

[3] J. T. Kindt and C. A. Schmuttenmaer, J. Chem. Phys. **110**(17), 8589 (1999).

[4] W. H. Press, S. A. Teukolsky, W. T. Vetterling, and B. P. Flannery, *Numerical Recipes in Fortran* (Cambridge Unversity Press, NewYork, 1986), second edition ed.

[5] H. J. Bakker, G. C. Cho, H. Kurz, Q. Wu, and X. C. Zhang, J. Opt. Soc. Am. B-Opt. Phys. **15**(6), 1795 (1998).

[6] G. Gallot, J. Q. Zhang, R. W. McGowan, T. I. Jeon, and D. Grischkowsky, Appl. Phys. Lett. **74**(23), 3450 (1999).

[7] M. C. Nuss, D. H. Auston, and F. Capasso, Phys. Rev. Lett. **58**(22), 2355 (1987).

[8] D. W. Bailey, C. J. Stanton, and K. Hess, Phys. Rev. B **42**(6), 3423 (1990).

[9] C. J. Stanton and D. W. Bailey, Phys. Rev. B **45**(15), 8369 (1992).

[10] M. Schall and P. U. Jepsen, Opt. Lett. **25**(1), 13 (2000).

[11] M. C. Beard and C. A. Schmuttenmaer, J. Chem. Phys. **114**(7), 2903 (2001).

[12] L. Brekhovskikh, *Waves in Layered Media* (Academic Press, New York, 1960).